Measurement of cold nuclear matter effects for inclusive J/ψ in p+Au collisions at $\sqrt{s_{\text{NN}}} = 200$ GeV

M. S. Abdallah[5], B. E. Aboona[55], J. Adam[6], L. Adamczyk[2], J. R. Adams[39],
J. K. Adkins[30], G. Agakishiev[28], I. Aggarwal[41], M. M. Aggarwal[41],
Z. Ahammed[60], I. Alekseev[3,35], D. M. Anderson[55], A. Aparin[28],
E. C. Aschenauer[6], M. U. Ashraf[11], F. G. Atetalla[29], A. Attri[41],
G. S. Averichev[28], V. Bairathi[53], W. Baker[10], J. G. Ball Cap[20], K. Barish[10],
A. Behera[52], R. Bellwied[20], P. Bhagat[27], A. Bhasin[27], J. Bielcik[14],
J. Bielcikova[38], I. G. Bordyuzhin[3], J. D. Brandenburg[6], A. V. Brandin[35],
I. Bunzarov[28], X. Z. Cai[50], H. Caines[63], M. Calderón de la Barca Sánchez[8],
D. Cebra[8], I. Chakaberia[31,6], P. Chaloupka[14], B. K. Chan[9], F-H. Chang[37],
Z. Chang[6], N. Chankova-Bunzarova[28], A. Chatterjee[11], S. Chattopadhyay[60],
D. Chen[10], J. Chen[49], J. H. Chen[18], X. Chen[48], Z. Chen[49], J. Cheng[57],
M. Chevalier[10], S. Choudhury[18], W. Christie[6], X. Chu[6], H. J. Crawford[7],
M. Csanád[16], M. Daugherity[1], T. G. Dedovich[28], I. M. Deppner[19],
A. A. Derevschikov[43], A. Dhamija[41], L. Di Carlo[62], L. Didenko[6], P. Dixit[22],
X. Dong[31], J. L. Drachenberg[1], E. Duckworth[29], J. C. Dunlop[6], N. Elsey[62],
J. Engelage[7], G. Eppley[45], S. Esumi[58], O. Evdokimov[12], A. Ewigleben[32],
O. Eyser[6], R. Fatemi[30], F. M. Fawzi[5], S. Fazio[6], P. Federic[38], J. Fedorisin[28],
C. J. Feng[37], Y. Feng[44], P. Filip[28], E. Finch[51], Y. Fisyak[6], A. Francisco[63],
C. Fu[11], L. Fulek[2], C. A. Gagliardi[55], T. Galatyuk[15], F. Geurts[45],
N. Ghimire[54], A. Gibson[59], K. Gopal[23], X. Gou[49], D. Grosnick[59], A. Gupta[27],
W. Guryn[6], A. I. Hamad[29], A. Hamed[5], Y. Han[45], S. Harabasz[15],
M. D. Harasty[8], J. W. Harris[63], H. Harrison[30], S. He[11], W. He[18], X. H. He[26],
Y. He[49], S. Heppelmann[8], S. Heppelmann[42], N. Herrmann[19], E. Hoffman[20],
L. Holub[14], Y. Hu[18], H. Huang[37], H. Z. Huang[9], S. L. Huang[52], T. Huang[37],
X. Huang[57], Y. Huang[57], T. J. Humanic[39], G. Igo[9,*], D. Isenhower[1],
W. W. Jacobs[25], C. Jena[23], A. Jentsch[6], Y. Ji[31], J. Jia[6,52], K. Jiang[48],
X. Ju[48], E. G. Judd[7], S. Kabana[53], M. L. Kabir[10], S. Kagamaster[32],
D. Kalinkin[25,6], K. Kang[57], D. Kapukchyan[10], K. Kauder[6], H. W. Ke[6],
D. Keane[29], A. Kechechyan[28], M. Kelsey[62], Y. V. Khyzhniak[35],
D. P. Kikoła[61], C. Kim[10], B. Kimelman[8], D. Kincses[16], I. Kisel[17], A. Kiselev[6],
A. G. Knospe[32], H. S. Ko[31], L. Kochenda[35], L. K. Kosarzewski[14],
L. Kramarik[14], P. Kravtsov[35], L. Kumar[41], S. Kumar[26],
R. Kunnawalkam Elayavalli[63], J. H. Kwasizur[25], R. Lacey[52], S. Lan[11],
J. M. Landgraf[6], J. Lauret[6], A. Lebedev[6], R. Lednicky[28,38], J. H. Lee[6],
Y. H. Leung[31], C. Li[49], C. Li[48], W. Li[45], X. Li[48], Y. Li[57], X. Liang[10],
Y. Liang[29], R. Licenik[38], T. Lin[49], Y. Lin[11], M. A. Lisa[39], F. Liu[11], H. Liu[25],
H. Liu[11], P. Liu[52], T. Liu[63], X. Liu[39], Y. Liu[55], Z. Liu[48], T. Ljubicic[6],
W. J. Llope[62], R. S. Longacre[6], E. Loyd[10], N. S. Lukow[54], X. F. Luo[11],
L. Ma[18], R. Ma[6], Y. G. Ma[18], N. Magdy[12], D. Mallick[36], S. Margetis[29],
C. Markert[56], H. S. Matis[31], J. A. Mazer[46], N. G. Minaev[43],
S. Mioduszewski[55], B. Mohanty[36], M. M. Mondal[52], I. Mooney[62],

D. A. Morozov[43], A. Mukherjee[16], M. Nagy[16], J. D. Nam[54], Md. Nasim[22],
K. Nayak[11], D. Neff[9], J. M. Nelson[7], D. B. Nemes[63], M. Nie[49],
G. Nigmatkulov[35], T. Niida[58], R. Nishitani[58], L. V. Nogach[43], T. Nonaka[58],
A. S. Nunes[6], G. Odyniec[31], A. Ogawa[6], S. Oh[31], V. A. Okorokov[35],
B. S. Page[6], R. Pak[6], J. Pan[55], A. Pandav[36], A. K. Pandey[58],
Y. Panebratsev[28], P. Parfenov[35], B. Pawlik[40], D. Pawlowska[61], C. Perkins[7],
L. Pinsky[20], R. L. Pintér[16], J. Pluta[61], B. R. Pokhrel[54], G. Ponimatkin[38],
J. Porter[31], M. Posik[54], V. Prozorova[14], N. K. Pruthi[41], M. Przybycien[2],
J. Putschke[62], H. Qiu[26], A. Quintero[54], C. Racz[10], S. K. Radhakrishnan[29],
N. Raha[62], R. L. Ray[56], R. Reed[32], H. G. Ritter[31], M. Robotkova[38],
O. V. Rogachevskiy[28], J. L. Romero[8], D. Roy[46], L. Ruan[6], J. Rusnak[38],
A. K. Sahoo[22], N. R. Sahoo[49], H. Sako[58], S. Salur[46], J. Sandweiss[63,*],
S. Sato[58], W. B. Schmidke[6], N. Schmitz[33], B. R. Schweid[52], F. Seck[15],
J. Seger[13], M. Sergeeva[9], R. Seto[10], P. Seyboth[33], N. Shah[24], E. Shahaliev[28],
P. V. Shanmuganathan[6], M. Shao[48], T. Shao[18], A. I. Sheikh[29], D. Y. Shen[18],
S. S. Shi[11], Y. Shi[49], Q. Y. Shou[18], E. P. Sichtermann[31], R. Sikora[2],
M. Simko[38], J. Singh[41], S. Singha[26], M. J. Skoby[44], N. Smirnov[63],
Y. Söhngen[19], W. Solyst[25], P. Sorensen[6], H. M. Spinka[4,*], B. Srivastava[44],
T. D. S. Stanislaus[59], M. Stefaniak[61], D. J. Stewart[63], M. Strikhanov[35],
B. Stringfellow[44], A. A. P. Suaide[47], M. Sumbera[38], B. Summa[42], X. M. Sun[11],
X. Sun[12], Y. Sun[48], Y. Sun[21], B. Surrow[54], D. N. Svirida[3], Z. W. Sweger[8],
P. Szymanski[61], A. H. Tang[6], Z. Tang[48], A. Taranenko[35], T. Tarnowsky[34],
J. H. Thomas[31], A. R. Timmins[20], D. Tlusty[13], T. Todoroki[58], M. Tokarev[28],
C. A. Tomkiel[32], S. Trentalange[9], R. E. Tribble[55], P. Tribedy[6],
S. K. Tripathy[16], T. Truhlar[14], B. A. Trzeciak[14], O. D. Tsai[9], Z. Tu[6],
T. Ullrich[6], D. G. Underwood[4,59], I. Upsal[45], G. Van Buren[6], J. Vanek[38],
A. N. Vasiliev[43], I. Vassiliev[17], V. Verkest[62], F. Videbæk[6], S. Vokal[28],
S. A. Voloshin[62], F. Wang[44], G. Wang[9], J. S. Wang[21], P. Wang[48], Y. Wang[11],
Y. Wang[57], Z. Wang[49], J. C. Webb[6], P. C. Weidenkaff[19], L. Wen[9],
G. D. Westfall[34], H. Wieman[31], S. W. Wissink[25], J. Wu[11], J. Wu[26], Y. Wu[10],
B. Xi[50], Z. G. Xiao[57], G. Xie[31], W. Xie[44], H. Xu[21], N. Xu[31], Q. H. Xu[49],
Y. Xu[49], Z. Xu[6], Z. Xu[9], C. Yang[49], Q. Yang[49], S. Yang[45], Y. Yang[37], Z. Ye[45],
Z. Ye[12], L. Yi[49], K. Yip[6], Y. Yu[49], H. Zbroszczyk[61], W. Zha[48], C. Zhang[52],
D. Zhang[11], J. Zhang[49], S. Zhang[12], S. Zhang[18], X. P. Zhang[57], Y. Zhang[26],
Y. Zhang[48], Y. Zhang[11], Z. J. Zhang[37], Z. Zhang[6], Z. Zhang[12], J. Zhao[44],
C. Zhou[18], X. Zhu[57], M. Zurek[4], M. Zyzak[17]

(STAR Collaboration)

[1] *Abilene Christian University, Abilene, Texas 79699*

[2] *AGH University of Science and Technology, FPACS, Cracow 30-059, Poland*

[3] *Alikhanov Institute for Theoretical and Experimental Physics NRC "Kurchatov Institute", Moscow 117218, Russia*

[4] *Argonne National Laboratory, Argonne, Illinois 60439*

[5] *American University of Cairo, New Cairo 11835, New Cairo, Egypt*

[6] *Brookhaven National Laboratory, Upton, New York 11973*

2

[7] *University of California, Berkeley, California 94720*

[8] *University of California, Davis, California 95616*

[9] *University of California, Los Angeles, California 90095*

[10] *University of California, Riverside, California 92521*

[11] *Central China Normal University, Wuhan, Hubei 430079*

[12] *University of Illinois at Chicago, Chicago, Illinois 60607*

[13] *Creighton University, Omaha, Nebraska 68178*

[14] *Czech Technical University in Prague, FNSPE, Prague 115 19, Czech Republic*

[15] *Technische Universität Darmstadt, Darmstadt 64289, Germany*

[16] *ELTE Eötvös Loránd University, Budapest, Hungary H-1117*

[17] *Frankfurt Institute for Advanced Studies FIAS, Frankfurt 60438, Germany*

[18] *Fudan University, Shanghai, 200433*

[19] *University of Heidelberg, Heidelberg 69120, Germany*

[20] *University of Houston, Houston, Texas 77204*

[21] *Huzhou University, Huzhou, Zhejiang 313000*

[22] *Indian Institute of Science Education and Research (IISER), Berhampur 760010 , India*

[23] *Indian Institute of Science Education and Research (IISER) Tirupati, Tirupati 517507, India*

[24] *Indian Institute Technology, Patna, Bihar 801106, India*

[25] *Indiana University, Bloomington, Indiana 47408*

[26] *Institute of Modern Physics, Chinese Academy of Sciences, Lanzhou, Gansu 730000*

[27] *University of Jammu, Jammu 180001, India*

[28] *Joint Institute for Nuclear Research, Dubna 141 980, Russia*

[29] *Kent State University, Kent, Ohio 44242*

[30] *University of Kentucky, Lexington, Kentucky 40506-0055*

[31] *Lawrence Berkeley National Laboratory, Berkeley, California 94720*

[32] *Lehigh University, Bethlehem, Pennsylvania 18015*

[33] *Max-Planck-Institut für Physik, Munich 80805, Germany*

[34] *Michigan State University, East Lansing, Michigan 48824*

[35] *National Research Nuclear University MEPhI, Moscow 115409, Russia*

[36] *National Institute of Science Education and Research, HBNI, Jatni 752050, India*

[37] *National Cheng Kung University, Tainan 70101*

[38] *Nuclear Physics Institute of the CAS, Rez 250 68, Czech Republic*

[39] *Ohio State University, Columbus, Ohio 43210*

[40] *Institute of Nuclear Physics PAN, Cracow 31-342, Poland*

[41] *Panjab University, Chandigarh 160014, India*

^{42} *Pennsylvania State University, University Park, Pennsylvania 16802*

^{43} *NRC "Kurchatov Institute", Institute of High Energy Physics, Protvino 142281, Russia*

^{44} *Purdue University, West Lafayette, Indiana 47907*

^{45} *Rice University, Houston, Texas 77251*

^{46} *Rutgers University, Piscataway, New Jersey 08854*

^{47} *Universidade de São Paulo, São Paulo, Brazil 05314-970*

^{48} *University of Science and Technology of China, Hefei, Anhui 230026*

^{49} *Shandong University, Qingdao, Shandong 266237*

^{50} *Shanghai Institute of Applied Physics, Chinese Academy of Sciences, Shanghai 201800*

^{51} *Southern Connecticut State University, New Haven, Connecticut 06515*

^{52} *State University of New York, Stony Brook, New York 11794*

^{53} *Instituto de Alta Investigación, Universidad de Tarapacá, Arica 1000000, Chile*

^{54} *Temple University, Philadelphia, Pennsylvania 19122*

^{55} *Texas A&M University, College Station, Texas 77843*

^{56} *University of Texas, Austin, Texas 78712*

^{57} *Tsinghua University, Beijing 100084*

^{58} *University of Tsukuba, Tsukuba, Ibaraki 305-8571, Japan*

^{59} *Valparaiso University, Valparaiso, Indiana 46383*

^{60} *Variable Energy Cyclotron Centre, Kolkata 700064, India*

^{61} *Warsaw University of Technology, Warsaw 00-661, Poland*

^{62} *Wayne State University, Detroit, Michigan 48201*

^{63} *Yale University, New Haven, Connecticut 06520*

* Deceased

Abstract

Measurement by the STAR experiment at RHIC of the cold nuclear matter (CNM) effects experienced by inclusive J/ψ at mid-rapidity in p+Au collisions at $\sqrt{s_{\mathrm{NN}}} = 200$ GeV is presented. Such effects are quantified utilizing the nuclear modification factor, $R_{p\mathrm{Au}}$, obtained by taking a ratio of J/ψ yield in p+Au collisions to that in p+p collisions scaled by the number of binary nucleon-nucleon collisions. The differential J/ψ yield in both p+p and p+Au collisions is measured through the dimuon decay channel, taking advantage of the trigger

4

capability provided by the Muon Telescope Detector in the RHIC 2015 run. Consequently, the J/ψ $R_{p\mathrm{Au}}$ is derived within the transverse momentum (p_T) range of 0 to 10 GeV/c. A suppression of approximately 30% is observed for $p_\mathrm{T} < 2$ GeV/c, while J/ψ $R_{p\mathrm{Au}}$ becomes compatible with unity for p_T greater than 3 GeV/c, indicating the J/ψ yield is minimally affected by the CNM effects at high p_T. Comparison to a similar measurement from 0-20% central Au+Au collisions reveals that the observed strong J/ψ suppression above 3 GeV/c is mostly due to the hot medium effects, providing strong evidence for the formation of the quark-gluon plasma in these collisions. Several model calculations show qualitative agreement with the measured J/ψ $R_{p\mathrm{Au}}$, while their agreement with the J/ψ yield in $p+p$ and $p+$Au collisions is worse.

Keywords: RHIC, cold nuclear matter effects, J/ψ suppression

---

1. Introduction

In ultra-relativistic heavy-ion collisions, a new state of matter, referred to as the Quark-Gluon Plasma (QGP), is created, in which the deconfined quarks and gluons are the relevant degrees of freedom. With the start of data-taking at the Relativistic Heavy Ion Collider (RHIC) in 2000 and the Large Hadron Collider (LHC) in 2010, tremendous progress has been made in understanding the properties of the QGP. Among various probes used to study the QGP, quarkonia play a unique role as they are expected to be dissociated by surrounding partons, i.e. gluons and quarks, if the medium temperature exceeds the melting temperature of the quarkonium states [1, 2]. Therefore, observations of quarkonium suppression in heavy-ion collisions have been considered strong evidence for QGP formation and important probes of the medium temperature, a fundamental property of the QGP. However, there are other effects that could modify the observed J/ψ yield in heavy-ion collisions, including the main contributions which are recombination and Cold Nuclear Matter (CNM) effects. The former refers to the J/ψ production mechanism arising from combination of deconfined charm and anti-charm quarks in the medium, while the latter is due to the par-

ticipation of nuclei in the collisions, but not as a result of the creation of the QGP.

As the most abundantly produced quarkonium state that is experimentally accessible, the J/ψ meson suppression in the QGP has been extensively measured at both RHIC and the LHC [3, 4, 5, 6, 7, 8, 9, 10, 11, 12, 13, 14]. At high transverse momentum ($p_{\mathrm{T}} > 5$ GeV/c), J/ψ mesons are strongly suppressed in central heavy-ion collisions, which is mainly attributed to the dissociation effect. In order to substantiate this conclusion, precise measurements of the CNM effects are needed to understand their potential contribution to the high-p_{T} J/ψ suppression observed in heavy-ion collisions. The CNM effects have been measured through collisions of a nucleus with a proton/deuteron at RHIC and with a proton at the LHC, in which the QGP is not expected to be produced [15, 16, 17, 18, 19, 20, 21]; or even if produced in such small system collisions, it is not expected to have a substantial effect. A general feature in these measurements is that a sizable suppression of the J/ψ yield, relative to that in $p+p$ collisions, is seen at low p_{T}, which gradually diminishes with increasing p_{T}. A hint of a mild enhancement is seen above 10 GeV/c at the LHC energies [19, 20]. Different physics mechanisms could contribute to the experimental observation. The nuclear parton distribution function (nPDF) is believed to be modified compared to the PDF of a free nucleon, e.g. a suppression (shadowing) at small Bjorken x and an enhancement (anti-shadowing) at intermediate x [22, 23]. Such a small-x effect, as well as the higher twist contribution [24], can be accounted for alternatively within the framework of the Color Glass Condensate (CGC) effective theory [25]. Before forming a bound state, the color-octet $c\bar{c}$ pairs could undergo energy loss within the cold nuclear matter of a nucleus [26]. After being formed, the bound-state J/ψ meson can break up through interactions with the nucleons in the nucleus [27] or due to interactions with co-moving soft particles produced in the same collisions [28]. It could also be possible that a small droplet of the QGP is formed in $p/d+$A collisions, leading to J/ψ dissociation [29, 30].

In this letter, the first measurement of the CNM effects experienced by

inclusive J/ψ at mid-rapidity in p+Au collisions at $\sqrt{s_{\mathrm{NN}}} = 200$ GeV with the Solenoidal Tracker At RHIC (STAR) experiment [31] is presented. They are quantified using the nuclear modification factor ($R_{p\mathrm{Au}}$):

$$R_{p\mathrm{Au}} = \frac{1}{\langle T_{\mathrm{AA}} \rangle} \times \frac{(\frac{d^2 N_{J/\psi}}{dp_{\mathrm{T}} dy})_{p+\mathrm{Au}}}{(\frac{d^2 \sigma_{J/\psi}}{dp_{\mathrm{T}} dy})_{p+p}} \tag{1}$$

where $(\frac{d^2 \sigma_{J/\psi}}{dp_{\mathrm{T}} dy})_{p+p}$ is the J/ψ cross section in p+p collisions and $(\frac{d^2 N_{J/\psi}}{dp_{\mathrm{T}} dy})_{p+\mathrm{Au}}$ is the invariant yield per inelastic p+Au collision. The nuclear thickness function $\langle T_{\mathrm{AA}} \rangle = \langle N_{\mathrm{coll}} \rangle / \sigma_{\mathrm{NN}}^{\mathrm{inel}}$ is calculated using a Glauber model [32], where $\sigma_{\mathrm{NN}}^{\mathrm{inel}} = 42$ mb [33] is the inelastic cross section of nucleon-nucleon collisions at 200 GeV, and $\langle N_{\mathrm{coll}} \rangle = 4.7 \pm 0.3$ is the average number of binary nucleon-nucleon collisions for 0-100% p+Au collisions [16]. The inclusive J/ψ sample used in this analysis includes both directly produced J/ψ as well as those from decays of excited charmonium states (approximately 40% [34]) and b-hadrons. Compared to previous measurements of $R_{d\mathrm{Au}}$ at RHIC [15, 17], the new $R_{p\mathrm{Au}}$ measurement has better precision over the entire kinematic range, especially for p_{T} larger than 3 GeV/c. This precision is partially achieved as the reference J/ψ cross section from p+p collisions was recorded the same year with the same trigger set-up and detector configuration as for the p+Au collisions, which allows for the partial cancelation of systematic uncertainties

2. Experiment, data set

Both the p+p and p+Au data samples used in this analysis were taken in 2015 by the STAR experiment at RHIC with the "dimuon" trigger. This trigger is dedicated to quarkonium measurements, and requires a coincidence signal in the east and west Vertex Position Detectors (VPD) [35] as well as two muon candidates in the Muon Telescope Detector (MTD) [36]. The VPD, made of plastic scintillators, covers full azimuth within the pseudorapidity (η) range of $4.24 < |\eta| < 5.1$, while the azimuthal coverage of the MTD, consisting of multigap resistive plate chambers, is about 45% within $|\eta| < 0.5$. A hit in the

MTD is classified as a muon candidate online if the difference between its arrival time measured by the MTD and the collision start time measured by the VPD falls within a pre-defined window. The sampled luminosities online are $122\,\mathrm{pb}^{-1}$ and $410\,\mathrm{nb}^{-1}$ for the $p{+}p$ and $p{+}$Au data sets, respectively.

The Time Projection Chamber (TPC) [37], encompassed in a uniform magnetic field of 0.5 T along the beam direction, is a gaseous detector for reconstructing a charged particle's trajectory, determining its momentum and measuring its specific energy loss (dE/dx) for particle identification (PID). It covers full azimuth within $|\eta| < 1.0$. Due to the high luminosity environment, most of reconstructed vertices are from out-of-time collisions from different bunch crossings than the triggered collision. The primary vertex is chosen such that its coordinate along the beam direction (v_z^{TPC}) is within 6 cm of the vertex z position reconstructed using the VPD (v_z^{VPD}), i.e. $|\Delta v_z| = |v_z^{\mathrm{TPC}} - v_z^{\mathrm{VPD}}| < 6$ cm, as the VPD is a fast detector and thus resilient to out-of-time collisions. Such a requirement is also effective in suppressing events in which more than one collision occurs in the same bunch crossing, since in such events the VPD picks up signals from all in-time collisions, resulting in an incorrectly reconstructed v_z^{VPD} that fails the $|\Delta v_z|$ requirement and is thus discarded. To further improve the vertex quality, there should be at least two tracks, which project to signals in the fast Barrel Electromagnetic Calorimeter (BEMC) [38] or cross the TPC central membrane, used in reconstructing the chosen primary vertex. Additionally, v_z^{TPC} is required to be within ± 100 cm of the center of the TPC, to ensure relatively uniform TPC acceptance while maximizing the sample statistics, and the primary vertex position along the radial direction should not exceed 1.5 cm to avoid selecting collisions between the beam and the beam pipe.

3. Analysis details

The invariant J/ψ yield per $p{+}p$ or $p{+}$Au collision is obtained by dividing the efficiency and acceptance corrected J/ψ yield by the number of minimum-bias (MB) events, equivalent to the analyzed dimuon triggered events. For the

$p+p$ analysis, the non-single diffractive cross section ($\sigma_{pp}^{\mathrm{NSD}} = 30.0 \pm 2.4$ mb [39]) at 200 GeV is used to convert the measured invariant yield to a cross section. For the $p+$Au analysis, the number of MB events is calculated using the MB triggered events which have the same trigger requirements as the dimuon trigger except for the condition of two muon candidates in the MTD.

3.1. J/ψ signal extraction

TPC tracks are chosen only if their Distance of Closest Approach (DCA) to the primary vertex is less than 3 cm. The primary vertex is then included in a refit of the track to improve the momentum resolution. To ensure good momentum and dE/dx resolutions, the number of TPC space points used for track reconstruction and dE/dx calculation are at least 20 and 15, respectively. The ratio of number of used to maximum possible TPC space points along the track trajectory should be no less than 0.52 to reject split tracks.

Tracks are further extrapolated radially to the middle of MTD modules, located at varying distances between 392.8 cm and 418.9 cm from the center of STAR, and matched to the closest MTD hits. If more than one track is matched to the same hit, the closest track is chosen. Once a track-hit association is established, the track is identified as a muon candidate when the following two criteria are satisfied: i) the associated MTD hit contributes to the dimuon trigger; ii) the pair survives the cut on a Likelihood Ratio (R) [40]. The R variable is defined as the following:

$$R = \frac{1-Y}{1+Y}, \ Y = \prod_i \frac{\mathrm{pdf}_i^{\mathrm{bkg}}}{\mathrm{pdf}_i^{\mathrm{sig}}} \tag{2}$$

where i stands for the five discriminating variables used, i.e., DCA, $\mathrm{n}\sigma_\pi$, $\Delta z/\sigma_{\Delta z}$, $\Delta y \times q/\sigma_{\Delta y \times q}$, Δt_{tof}, and $\mathrm{pdf}_i^{\mathrm{sig}}$, and $\mathrm{pdf}_i^{\mathrm{bkg}}$ are the probability distribution functions of each variable for signal muons and background particles. The normalized energy loss is defined as $\mathrm{n}\sigma_\pi = \frac{\ln(dE/dx)_{\mathrm{measured}} - \ln(dE/dx)_{\mathrm{theory}}^\pi}{\sigma(\ln(dE/dx))}$. Here $(dE/dx)_{\mathrm{measured}}$ is the measured energy loss in the TPC, $(dE/dx)_{\mathrm{theory}}^\pi$ is the expected energy loss for a pion based on the Bichsel formalism [41], and $\sigma(\ln(dE/dx))$

is the resolution of the $\ln(dE/dx)$ measurement. The shape of the $n\sigma_\pi$ distribution is expected to be independent of track $p_{\rm T}$. Δz and Δy are the position differences between the projected track trajectories on the MTD and the associated MTD hits along the z and azimuthal directions, and Δy is multiplied by the track's electric charge (q) to eliminate the difference between positively and negatively charged particles. These two variables are divided by their resolutions to remove their $p_{\rm T}$ dependences. Finally, $\Delta t_{\rm tof}$ represents the difference between the measured and expected flight time for a muon flying from the primary vertex to the MTD. The measured flight time is based on the MTD and VPD information, while the expected value is obtained by dividing the track flight length by its speed. The probability distribution functions for signal muons and background particles are extracted from data. The signal muon sample is obtained from muon candidate pairs of unlike charge signs ("unlike-sign") around the J/ψ mass range ($3.0 < M_{\mu^+\mu^-} < 3.2$ GeV/c^2) after subtracting the muon candidate pairs of like charge signs ("like-sign"), where the muon candidates are identified without applying the PID cut in question. The like-sign pairs of muon candidates are used as background particles. The value of R is expected to approach 1 for signal muons, and -1 for background. For example, the distributions of R for signal muons and background particles above 1.3 GeV/c are shown in Fig. 1 from the $p+p$ data sample. A clear separation between signal and background is seen. The optimal cut of $R > -0.65$, independent of muon $p_{\rm T}$, is determined by maximizing the J/ψ signal significance in the entire $p_{\rm T}$ range, and is shown as the vertical dashed line in Fig. 1. The optimal cut is determined to be $R > -0.01$ for the $p+$Au analysis.

The invariant mass distributions for unlike-sign muon candidate pairs, integrated over $p_{\rm T}$, are shown in Fig. 2 as filled circles for $p+p$ (left) and $p+$Au (right) events. For each unlike-sign pair, one of the muon candidates should have a $p_{\rm T}$ above 1.5 GeV/c, while the other above 1.3 GeV/c. The pair rapidity is within $|y| < 0.5$. The combinatorial background is estimated using like-sign TPC track pairs without matching to the MTD, which are scaled to the invariant mass distributions of like-sign muon candidate pairs and corrected
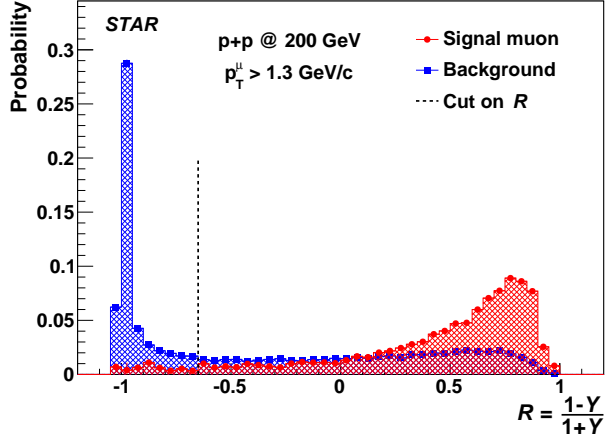
Figure 1: R distribution for signal muons (circles) and background (squares) in p+p analysis. The dashed vertical line indicates the cut to select muon candidates.
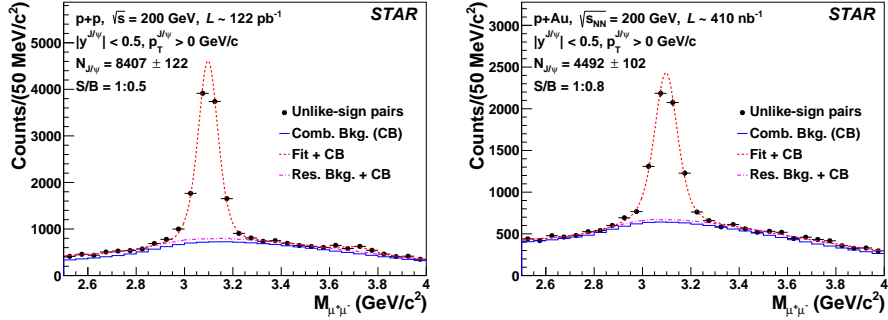

Figure 2: Invariant mass distributions of unlike-sign muon pairs (filled circles) in p+p (left) and p+Au (right) collisions. These distributions, after subtracting the combinatorial background (CB, blue histograms), are fit with a Student's t function describing the signal and a first-order polynomial function representing the residual background. The resulting combined (dashed lines) and residual background (dot-dashed lines) fits are also shown with the combinatorial background. Horizontal and vertical bars around data points depict bin width and statistical errors, respectively.

11

for the MTD acceptance difference for like-sign and unlike-sign pairs. Such an acceptance difference is evaluated using the ratio of unlike-sign to like-sign muon candidate pairs from mixed events, i.e. the two muons in a pair are taken from different events, using 200 GeV Au+Au collisions recorded in 2014 [6]. To extract the raw J/ψ yield, the unlike-sign invariant mass distribution, with the combinatorial background subtracted, is fit with the sum of a Student's t function representing the J/ψ signal and a first-order polynomial function describing the residual background, using the minimum χ^2 method. The normality parameter in the Student's t function, which determines to what extent its tail is enhanced with respect to a Gaussian function, is fixed according to simulations. Fit results for signal plus residual background and residual background only are shown as dashed and dot-dashed lines in Fig. 2 with the combinatorial background added back. This procedure is applied to the J/ψ signal extraction for p_T below 4 GeV/c. For p_T greater than 4 GeV/c, where the signal-to-background ratio increases and the statistics decreases, the unlike-sign distributions, without background subtraction, are directly fit with a Student's t function plus a first-order polynomial function using the maximum likelihood method. The signal-to-background ratios listed in Fig. 2 are calculated within $3.0 < M_{\mu^+\mu^-} < 3.2$ GeV/c^2.

3.2. Efficiency and acceptance correction

The TPC tracking efficiency and acceptance are evaluated through an embedding procedure. Simulated $J/\psi \to \mu^+\mu^-$ processes are propagated through the STAR detector simulation using the GEANT3 package [42]. They are then mixed with randomly sampled dimuon triggered real events, and reconstructed the same way as real data. The embedded J/ψ is assumed to have zero polarization [43]. The TPC tracking efficiency is 86% (85.5%) independent of muon p_T above 1.3 GeV/c for p+p (p+Au) data. An additional inefficiency observed in the data for one of the TPC sectors is applied to the embedding sample.

The MTD matching efficiency for muons includes contributions from the MTD acceptance and the response efficiency of each MTD module, which is

defined as the probability for a track to generate a hit in the module when extrapolated to the active volume. The MTD acceptance is simulated in the aforementioned embedding sample, while the response efficiencies are assessed using cosmic ray data. For MTD modules residing at the bottom hemisphere of the STAR detector, the response efficiencies as a function of muon p_T are obtained by extrapolating cosmic ray tracks to the active volume and finding the fraction of tracks matched to MTD hits. The average response efficiency of all bottom modules is also used as a template for MTD modules located at the top hemisphere, for which the cosmic rays travel from outside in, which is the opposite from the real collision data. The absolute scale of the template is determined by matching to the response efficiency of each top module at $p_\mathrm{T} > 5$ GeV/c, where the efficiency reaches a plateau. The extracted response efficiency for each MTD module is then applied to the embedding sample. The resulting MTD matching efficiencies for bottom modules evaluated using the embedding sample and the cosmic ray data are consistent with each other. To take into account the residual differences, the ratio between the average of the two and the matching efficiency from embedding is used as an additional scale factor for obtaining the final MTD matching efficiency for all the modules. Furthermore, half of the difference between the two, ranging between 0 and 6.5%, is taken as a source of systematic uncertainty. This procedure applies equally to both $p+p$ and $p+$Au analyses.

The MTD trigger efficiency consists of three components: trigger electronics efficiency, trigger timing window cut efficiency and trigger patch configuration efficiency. The first two components are evaluated using MB triggered event samples for which only the coincidence signal in east and west VPD is required. The probability for a muon candidate to generate a correct signal in the trigger electronics and pass the trigger timing window cut is found to be close to 100% for both $p+p$ and $p+$Au data. The third component arises from the fact that the dimuon trigger requires signals from distinct trigger patches while the muon daughters from high-p_T J/ψ decays are highly boosted and could hit the same MTD trigger patch. Since this component is driven by the MTD geometry

and the J/ψ decay kinematics, the embedding sample is utilized. The resulting efficiency is mostly 100% until J/ψ p_T of 5 GeV/c, and decreases to about 95% at 8-10 GeV/c.

The muon PID efficiency associated with the cut on R is estimated using a tag-and-probe method based on real data. For each unlike-sign pair of TPC tracks matched to the MTD, one muon is randomly selected as the *tag* muon while the other the *probe* muon. For the tag muon, a strict cut of $R > 0.25$ is applied to increase the signal-to-background ratio. For the probe muon, two cases are tried, i.e., no cut on R and the default cut on R. The J/ψ counts in each probe muon p_T bin are extracted for the two cases, and the ratio is parametrized as the muon PID efficiency. In the $p+p$ analysis, the muon PID efficiency increases from 90% at 1.3 GeV/c to 98% above 5 GeV/c, while it increases from 69% at 1.3 GeV/c to 96% above 5 GeV/c for $p+$Au analysis due to the tighter cut applied.

The VPD trigger and vertex finding efficiencies are obtained by embedding PYTHIA [44, 45] (HIJING [46]) events, after passing through the GEANT simulation of the STAR detector, into zero-bias $p+p$ ($p+$Au) events. The zero-bias events were taken without any trigger requirement at random times. For the $p+p$ analysis, both the MB PYTHIA events and PYTHIA events containing a J/ψ within $|y| < 0.5$ are used for embedding. The former is needed for calculating the equivalent number of MB events corresponding to the analyzed dimuon triggered events. Two different PYTHIA configurations: i) PYTHIA 6.4.28 [44] plus the Perugia2012 tune [47]; ii) PYTHIA 8.1.62 [45] with the STAR heavy flavor tune [48], are used as they bracket the measured multiplicity distribution of J/ψ events [49]. To account for the apparent differences between data and PYTHIA, event multiplicity distributions for both MB [50] and J/ψ events [49] are then used to weight the embedding samples. The VPD efficiency for events containing a J/ψ decreases with increasing J/ψ p_T, arising due to the decreased amount of energy available for producing particles in the VPD acceptance in these events. The average efficiencies of the two PYTHIA configurations are taken as the central values, while half the difference of the two is

14

taken as a source of systematic uncertainties. For the p+Au analysis, a similar procedure is used except that the HIJING event generator [46] is employed. Since no quarkonium production is implemented, HIJING events containing a D^0 meson within $|y| < 0.5$ are used for embedding, which is validated by the good agreement seen between the efficiencies extracted from embedding J/ψ and D^0 PYTHIA events. The event multiplicity as a function of pseudorapidity in HIJING p+Au events is compared to the PHOBOS measurement for d+Au collisions [51] scaled by the difference in N_{part} between p+Au and d+Au collisions. Here N_{part} refers to the number of participating nucleons in a p+Au or d+Au collision. These results agree for both mid-rapidity and the p-going side. However, on the Au-going side HIJING significantly underpredicts the particle multiplicity, and therefore the VPD efficiency in this side is also assumed to be 100% as an upper limit. The average VPD efficiency in the Au-going side from the default HIJING and the upper limit is taken as the central value, while half of the difference is taken as the uncertainty.

3.3. Systematic uncertainties

Systematic uncertainties due to different aspects of the analysis procedure are evaluated. For the signal extraction, the following variations are evaluated. When determining the combinatorial background scaling, a first-order polynomial function is used and the fitting range is varied from [2.5, 4.0] GeV/c^2 to [2.3, 4.2] GeV/c^2 and [2.55, 3.9] GeV/c^2. When fitting the invariant mass distributions, the fitting range is changed by 0.3 to 0.6 GeV/c^2 depending on the J/ψ p_{T}, a second-order polynomial function is used for fitting the residual background, and the binning for the invariant mass distribution is varied from 50 (80) MeV/c^2 to 20 (50) MeV/c^2 for $p_{\mathrm{T}} <$ ($>$) 3.5 GeV/c. The simulation uncertainty in the normality parameter is also taken into account. Furthermore, J/ψ yields are extracted by counting the unlike-sign muon candidate pairs around J/ψ mass after background subtraction. The maximum deviations from the default cases are taken as the uncertainties. The uncertainty in the TPC tracking efficiency is evaluated by changing the number of TPC space

points used for track reconstruction and dE/dx calculation from 20 and 15 to 25 and 20 or 15 and 10 simultaneously in data analysis and efficiency estimation, and the resulting changes in the final results are used as the systematic uncertainty. It is 4% independent of J/ψ p_{T} for both $p+p$ and $p+$Au analyses. In terms of the MTD matching efficiency, its uncertainty includes three contributions: i) statistical precision of the cosmic ray data used to determine the MTD response efficiencies; ii) the uncertainty arising from using the response efficiency template for the top MTD modules which is estimated as the average absolute differences between the response efficiency template and the actual response efficiencies for bottom MTD modules; iii) half of the difference in the matching efficiencies between using cosmic ray data and the embedding sample. The uncertainty decreases from 6.0% at a J/ψ p_{T} of 1 GeV/c to 1.9% at 10 GeV/c. For both the muon PID and MTD trigger efficiencies, their uncertainties are driven by the statistical precision of the data-driven methods used. Systematic uncertainties associated with the VPD trigger and vertex finding efficiencies include the following three contributions: statistical precision of the embedding sample, deviations between different PYTHIA or HIJING configurations and the central value, and the variation in the VPD response efficiency from 100% to 90%. The former is uncorrelated among different p_{T} bins, while the latter two are independent of p_{T} and included in the global uncertainties. The impact of remaining pileup contribution to the J/ψ yield is estimated to be 2.7% and 1.3% for $p+p$ and $p+$Au analyses, respectively, and assigned as a source of uncertainty. Finally, an 8% uncertainty on $\sigma_{pp}^{\mathrm{NSD}}$ is added. For the $R_{p\mathrm{Au}}$ measurement, the uncertainties of the TPC tracking efficiency, MTD matching efficiency and pileup contribution mostly cancel, while other sources of uncertainties are uncorrelated between $p+p$ and $p+$Au analyses and thus added in quadrature. All the individual sources of uncertainties are listed in Table 1, along with the total uncertainties obtained by adding individual ones in quadrature. Global uncertainties, referred to in later sections, include those from the p_{T}-independent part in VPD trigger and vertex finding efficiencies, pileup contribution, $\sigma_{pp}^{\mathrm{NSD}}$ and N_{coll}.

Uncertainty source	$p+p$	$p+\mathrm{Au}$	$R_{p\mathrm{Au}}$
Signal extraction	1.1 - 8.5%	2.1 - 6.0%	2.7-10.4%
TPC tracking	4%	4%	cancelled
MTD matching	1.9 - 5.5%	1.9 - 6.0%	negligible
Muon PID	0.9 - 1.2%	3.0 - 4.8%	3.1 - 4.9 %
MTD trigger	1.4%	1.4%	2%
VPD trigger and vertex finding	9.3 - 15.2%	1.3 - 7.8%	9.4 - 17.1%
Pileup	2.7%	1.3%	1.4%
$\sigma_{pp}^{\mathrm{NSD}}$	8%	-	8%
N_{coll}	-	-	6.4%
Total	13.5 - 20.0%	6.7 - 11.5%	14.8%-22.9%

Table 1: List of individual and total systematic uncertainties.

4. Results and discussions

The differential cross section of inclusive J/ψ times the branching ratio within $|y| < 0.5$ in $p+p$ collisions at $\sqrt{s} = 200$ GeV is shown in the top panel of Fig. 3 as a function of p_{T}. The data points are placed at the p_{T} positions whose yields are equal to the average yields of the corresponding bins [52]. For this purpose, the following empirical function is used to fit the differential cross section as a function of p_{T} iteratively:

$$f(p_{\mathrm{T}}) = A \times p_{\mathrm{T}} \times (1 + (p_{\mathrm{T}}/B)^2)^C, \tag{3}$$

where A, B and C are free parameters. The integrated J/ψ cross section per unity rapidity is:

$$\mathrm{Br}_{\mu\mu}\frac{\mathrm{d}\sigma_{J/\psi}}{\mathrm{d}y}|_{y=0} = 43.9 \pm 0.7(stat.) \pm 6.1(syst.) \text{ nb} \tag{4}$$

To facilitate the comparison of this measurement to previous publications, Eq. 3 is used to fit the differential J/ψ cross section, and the fit result is shown as the dashed line in the top panel of Fig. 3. Ratios of the current and previous
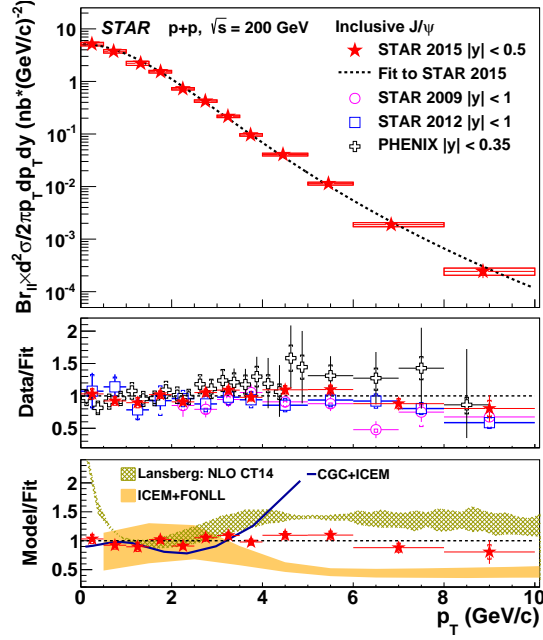
Figure 3: Top: inclusive J/ψ cross section (red stars) as a function of p_T in $p+p$ collisions at $\sqrt{s}$ = 200 GeV, with a fit to the result shown as the dashed line. The vertical error bars, smaller than the marker size, and open boxes around data points represent statistical errors and systematic uncertainties. The horizontal error bars indicate the bin width. Middle: ratios of current and previous measurements [3, 49, 34] to the fit. The vertical error bars and brackets around data points represent statistical errors and systematic uncertainties. Global uncertainties are not shown for all the measurements. Bottom: ratios of current measurement and different model calculations [53, 54, 55, 56, 57, 58] to the fit. Systematic uncertainties on data points are smaller than the marker size.

results of different rapidity coverages [3, 49, 34] to the fit function are shown in the middle panel of Fig. 3. Based on calculations of the Improved Color Evaporation Model (ICEM) [53], which is described below, the invariant J/ψ yields within $|y| < 0.5$ and $|y| < 0.35$ agree with each other within 2% while the yield within $|y| < 0.5$ is about 6% (11%) larger at 0 (10) GeV/c than that within $|y| < 1$. This indicates that the different STAR analyses are consistent with one another, while the new measurement improves the precision below 1 GeV/c. On the other hand, while the PHENIX measurement is also consistent with this analysis within uncertainties, its central values are systematically higher above 2.5 GeV/c. Ratios of three model calculations to the fit are shown in the lower panel of Fig. 3, and compared to data. The ICEM determines the transition probability from $c\bar{c}$ pairs to J/ψ by fitting to J/ψ measurements from previous publications [53]. The associated uncertainties arise from varying the charm quark mass (m_c), factorization and renormalization scales. For the calculation labelled as "CGC+ICEM", it utilizes the CGC framework to obtain the $c\bar{c}$ production cross section and the ICEM for hadronization. Since the variation in m_c between 1.3 and 1.4 GeV/c^2 leads to negligible differences in this work, only the results with $m_c = 1.3$ GeV/c^2 are compared to data. The model calculation from Lansberg is based on the CT14 proton PDF at Next-to-Leading Order (NLO) [59] and its uncertainties are dominated by variations in the factorization scale. Both "CGC+ICEM" and Lansberg calculations are tuned to previous inclusive J/ψ cross section measurement at 200 GeV [34], and therefore can be directly compared to this measurement. The ICEM calculation includes only prompt J/ψ, i.e. directly produced J/ψ plus those from decays of excited charmonium states. The contribution to J/ψ from b-hadrons is calculated at Fixed Order plus Next-to-Leading Logarithms (FONLL) [60, 61] and added to the ICEM result. The b-hadron feeddown contribution increases from less than 1% below 1 GeV/c to approximately 9% at 10 GeV/c. Uncertainties of the FONLL calculation are added in quadrature to ICEM model uncertainties. The ICEM and "CGC+ICEM" results agree with the data within uncertainties up to about 3.5 GeV/c before diverging from the data. The Lansberg calculation

19

is consistently above the data, especially for $p_\mathrm{T} < 0.5$ GeV/c.

The inclusive J/ψ yield times the branching ratio as a function of p_T in p+Au collisions at $\sqrt{s_\mathrm{NN}} = 200$ is shown in Fig. 4, top panel. Similarly, the yield is fit with Eq. 3, which is shown as the dashed line. Ratios of the data and different model calculations to the fit are shown in the bottom panel of Fig. 4. The ICEM
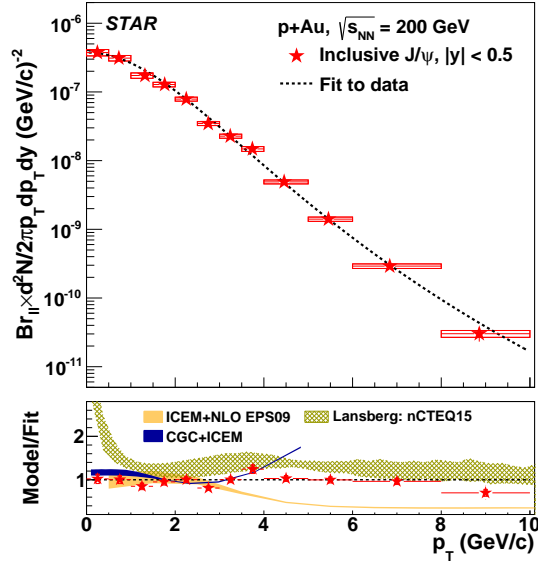

Figure 4: Top: inclusive J/ψ yield (red stars) as a function of p_T in p+Au collisions at $\sqrt{s_\mathrm{NN}}$ = 200 GeV, with a fit to the result shown as the dashed line. The vertical error bars, smaller than the marker size, and open boxes around data points represent statistical errors and systematic uncertainties. The horizontal error bars indicate the bin width. Bottom: ratios of data and different model calculations [53, 54, 55, 56, 57, 58] to the fit. Systematic uncertainties on data points are smaller than the marker size.

utilizes the NLO EPS09 nPDF [62], while the CGC+ICEM approach directly calculates the $c\bar{c}$ production cross section in p+Au collisions based on the CGC formalism. The uncertainties for the former arise from the nPDF uncertainties, while for the latter the main contributions are the variations of the average momentum of soft color exchanges and the scale factor between the saturation scales for proton and Au nucleus. In the Lansberg calculation, the nCTEQ15 nPDF at NLO [22], constrained by the J/ψ measurements at the LHC, is used

[55, 56, 57, 58]. The systematic uncertainty band of the Lansberg calculation includes the nPDF uncertainty at 68% confidence level as well as variations on the factorization scale. Very similar results, not shown here, are obtained using the EPPS16 nPDF at NLO [23] within the same framework. The comparison between data and model calculations is similar to that seen for p+p collisions, even though the contribution of b-hadron decayed J/ψ is not included in the model calculations for p+Au collisions.

Following Eq. 1, the inclusive J/ψ $R_{p\mathrm{Au}}$, quantifying the CNM effects on J/ψ production in 200 GeV p+Au collisions, is calculated and shown as a function of p_T in the top panel of Fig. 5. The global uncertainty is shown as the filled box at unity. A suppression of approximately 30% is seen below 2 GeV/c,
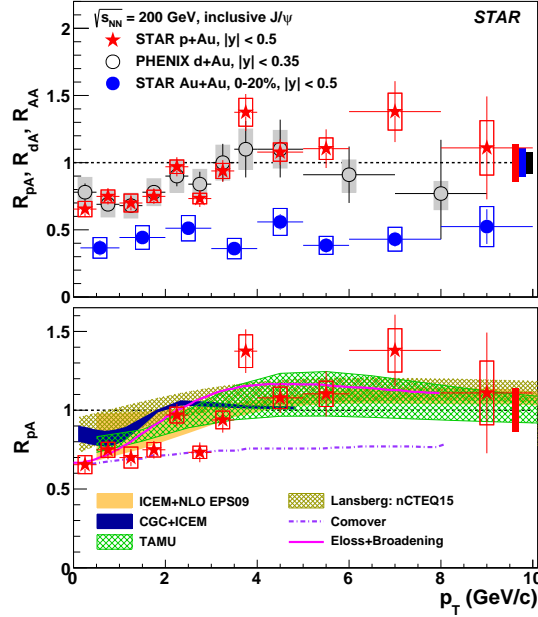
Figure 5: Top: inclusive J/ψ $R_{p\mathrm{Au}}$ (filled stars) and $R_{d\mathrm{Au}}$ (open circles) [17] as a function of p_T compared to the J/ψ R_{AA} (filled circles) measured in 0-20% central Au+Au collisions at $\sqrt{s_{\mathrm{NN}}}$ = 200 GeV. The error bars and open boxes around data points represent statistical errors and systematic uncertainties, while the filled boxes at unity display the global uncertainties for each data set. Bottom: comparison of J/ψ $R_{p\mathrm{Au}}$ to different model calculations [26, 28, 29, 30, 53, 54, 55, 56, 57, 58].

which gradually goes away as p_T increases. For p_T above 3 GeV/c, the J/ψ $R_{p\mathrm{Au}}$ becomes consistent with unity, indicating little CNM effects on the J/ψ production in this kinematic range. The inclusive J/ψ $R_{d\mathrm{Au}}$ [17] in d+Au collisions at $\sqrt{s_{\mathrm{NN}}} = 200$ GeV is shown as open circles for comparison. It agrees with the J/ψ $R_{p\mathrm{Au}}$ within uncertainties, indicating that the CNM effects in p+Au and d+Au collisions are similar. It is worth noting that the new J/ψ $R_{p\mathrm{Au}}$ has a better precision than the published J/ψ $R_{d\mathrm{Au}}$ in the entire p_T range. Also shown in the panel as filled circles are the J/ψ R_{AA} measured in 0-20% central Au+Au collisions at $\sqrt{s_{\mathrm{NN}}} = 200$ GeV [6], in which the J/ψ yield is seen to be suppressed over the entire p_T range. For $p_T < 2$ GeV/c, the CNM effects contribute significantly to the J/ψ suppression seen in heavy-ion collisions, while for $p_T > 3$ GeV/c, the dissociation effect arising from the presence of the QGP medium is mainly responsible for the strong suppression. Different model calculations are shown in the bottom panel of Fig. 5, and compared to the data. The ICEM and Lansberg calculations include only nPDF effects based on EPS09 [62] and nCTEQ15 [22] parameterizations, respectively. The TAMU model extends the transport model for heavy-ion collisions to p+Au collisions [29, 30]. In this model, the NLO EPS09 nPDF is utilized [62], and the short-lived hot medium modifies the observed J/ψ yields in p+Au collisions through both dissociation and recombination. Uncertainties of this calculation includes nPDF uncertainties, variation of the broadening parameter for incorporating the Cronin effect, and uncertainties in the formation times for both the QGP and J/ψ meson. In another model, shown as the solid line and labelled as "Eloss+Broadening", interactions between fast-moving color-octet $c\bar{c}$ pairs in the nucleus rest frame and the cold nuclear medium induce both radiative energy loss and p_T-broadening [26]. The latter is responsible for the J/ψ enhancement above 2.5 GeV/c. A comover model, introducing breakup of J/ψ mesons through interactions with final state particles traveling along with J/ψ, is shown as the dot-dashed line in the panel [28]. The nPDF effect is also included in the comover model, based on leading-order EPS09 parameterization. All the model calculations are consistent with data within theoretical and experimental uncertainties. It is worth

22

noting that the comover model underpredicts data above 3.5 GeV/c by 2.3σ.

5. Summary

In summary, the inclusive J/ψ yields within $|y| < 0.5$ are measured in p+p and p+Au collisions at $\sqrt{s_{\mathrm{NN}}} = 200$ GeV through the dimuon decay channel using the STAR experiment. Both data samples were taken with the MTD dimuon trigger in 2015. The differential J/ψ cross section in p+p collisions is consistent with previous results, and the data precision for $p_{\mathrm{T}} < 1$ GeV/c is significantly improved for STAR measurements. For the first time, the J/ψ $R_{p\mathrm{Au}}$ is measured within $0 < p_{\mathrm{T}} < 10$ GeV/c to quantify the CNM effects experienced by the J/ψ meson in p+Au collisions. It increases from 0.67 at 0-1 GeV/c to be consistent with unity above 3 GeV/c. Comparison to a similar measurement in 0-20% central Au+Au collisions at $\sqrt{s_{\mathrm{NN}}} = 200$ GeV confirms that the observed large suppression of the J/ψ yield above 3 GeV/c is mostly caused by hot medium effects, providing strong evidence of the QGP formation in these collisions. Model calculations including different underlying physics mechanisms can qualitatively describe the data within uncertainties. The new measurements presented in this paper provide an improved reference for interpreting similar measurements in 200 GeV Au+Au collisions, and will further constrain model calculations of the CNM effects for J/ψ at RHIC.

References

References

[1] T. Matsui, H. Satz, J/ψ Suppression by Quark-Gluon Plasma Formation, Phys. Lett. B178 (1986) 416–422. `doi:10.1016/0370-2693(86)91404-8`.

[2] A. Andronic, et al., Heavy-flavour and quarkonium production in the LHC era: from proton–proton to heavy-ion collisions, Eur. Phys. J. C76 (2016) 107. `arXiv:1506.03981`, `doi:10.1140/epjc/s10052-015-3819-5`.

[3] L. Adamczyk, et al., J/ψ production at high transverse momenta in $p + p$ and Au+Au collisions at $\sqrt{s_{NN}} = 200$ GeV, Phys. Lett. B722 (2013) 55–62. `arXiv:1208.2736`, `doi:10.1016/j.physletb.2013.04.010`.

[4] L. Adamczyk, et al., J/ψ production at low p_T in Au+Au and Cu+Cu collisions at $\sqrt{s_{NN}} = 200$ GeV with the STAR detector, Phys. Rev. C90 (2014) 024906. `arXiv:1310.3563`, `doi:10.1103/PhysRevC.90.024906`.

[5] L. Adamczyk, et al., Energy dependence of J/ψ production in Au+Au collisions at $\sqrt{s_{NN}} = 39$, 62.4 and 200 GeV, Phys. Lett. B771 (2017) 13–20. `arXiv:1607.07517`, `doi:10.1016/j.physletb.2017.04.078`.

[6] J. Adam, et al., Measurement of inclusive J/ψ suppression in Au+Au collisions at $\sqrt{s_{NN}} = 200$ GeV through the dimuon channel at STAR, Phys. Lett. B797 (2019) 134917. arXiv:1905.13669, doi:10.1016/j.physletb. 2019.134917.

[7] A. Adare, et al., J/ψ Production vs Centrality, Transverse Momentum, and Rapidity in Au+Au Collisions at $\sqrt{s_{NN}} = 200$ GeV, Phys. Rev. Lett. 98 (2007) 232301. arXiv:nucl-ex/0611020, doi:10.1103/PhysRevLett. 98.232301.

[8] A. Adare, et al., J/ψ suppression at forward rapidity in Au+Au collisions at $\sqrt{s_{NN}} = 200$ GeV, Phys. Rev. C84 (2011) 054912. arXiv:1103.6269, doi:10.1103/PhysRevC.84.054912.

[9] J. Adam, et al., Inclusive, prompt and non-prompt J/ψ production at midrapidity in Pb-Pb collisions at $\sqrt{s_{\mathrm{NN}}} = 2.76$ TeV, JHEP 07 (2015) 051. arXiv:1504.07151, doi:10.1007/JHEP07(2015)051.

[10] J. Adam, et al., Differential studies of inclusive J/ψ and $\psi(2S)$ production at forward rapidity in Pb-Pb collisions at $\sqrt{s_{\mathrm{NN}}} = 2.76$ TeV, JHEP 05 (2016) 179. arXiv:1506.08804, doi:10.1007/JHEP05(2016)179.

[11] J. Adam, et al., J/ψ suppression at forward rapidity in Pb-Pb collisions at $\sqrt{\mathbf{s_{\mathrm{NN}}}} = \mathbf{5.02}$ TeV, Phys. Lett. B766 (2017) 212–224. arXiv:1606.08197, doi:10.1016/j.physletb.2016.12.064.

[12] V. Khachatryan, et al., Suppression and azimuthal anisotropy of prompt and nonprompt J/ψ production in PbPb collisions at $\sqrt{s_{\mathrm{NN}}} = 2.76$ TeV, Eur. Phys. J. C77 (2017) 252. arXiv:1610.00613, doi:10.1140/epjc/ s10052-017-4781-1.

[13] A. M. Sirunyan, et al., Measurement of prompt and nonprompt charmonium suppression in PbPb collisions at 5.02 TeV, Eur. Phys. J. C78 (2018) 509. arXiv:1712.08959, doi:10.1140/epjc/s10052-018-5950-6.

[14] M. Aaboud, et al., Prompt and non-prompt J/ψ and $\psi(2S)$ suppression at high transverse momentum in 5.02 TeV Pb+Pb collisions with the ATLAS experiment, Eur. Phys. J. C78 (9) (2018) 762. `arXiv:1805.04077, doi:10.1140/epjc/s10052-018-6219-9`.

[15] L. Adamczyk, et al., J/ψ production at low transverse momentum in p+p and d+Au collisions at $\sqrt{s_{NN}}$ = 200 GeV, Phys. Rev. C93 (6) (2016) 064904. `arXiv:1602.02212, doi:10.1103/PhysRevC.93.064904`.

[16] U. Acharya, et al., Measurement of J/ψ at forward and backward rapidity in $p + p$, $p + Al$, $p + Au$, and ^{3}He+Au collisions at $\sqrt{s_{NN}}$ = 200 GeV, Phys. Rev. C 102 (1) (2020) 014902. `arXiv:1910.14487, doi:10.1103/PhysRevC.102.014902`.

[17] A. Adare, et al., Transverse-Momentum Dependence of the J/ψ Nuclear Modification in d+Au Collisions at $\sqrt{s_{NN}}$ = 200 GeV, Phys. Rev. C 87 (3) (2013) 034904. `arXiv:1204.0777, doi:10.1103/PhysRevC.87.034904`.

[18] S. Acharya, et al., Prompt and non-prompt J/ψ production and nuclear modification at mid-rapidity in p–Pb collisions at $\sqrt{\mathbf{s_{NN}}}$ = **5.02** TeV, Eur. Phys. J. C78 (6) (2018) 466. `arXiv:1802.00765, doi:10.1140/epjc/s10052-018-5881-2`.

[19] M. Aaboud, et al., Measurement of quarkonium production in proton–lead and proton–proton collisions at 5.02 TeV with the ATLAS detector, Eur. Phys. J. C78 (2018) 171. `arXiv:1709.03089, doi:10.1140/epjc/s10052-018-5624-4`.

[20] A. M. Sirunyan, et al., Measurement of prompt and nonprompt J/ψ production in pp and pPb collisions at $\sqrt{s_{NN}}$ = 5.02 TeV, Eur. Phys. J. C77 (4) (2017) 269. `arXiv:1702.01462, doi:10.1140/epjc/s10052-017-4828-3`.

[21] S. Acharya, et al., Inclusive J/ψ production at forward and backward rapidity in p-Pb collisions at $\sqrt{s_{NN}}$ = 8.16 TeV, JHEP 07 (2018) 160. `arXiv:1805.04381, doi:10.1007/JHEP07(2018)160`.

[22] K. Kovarik, et al., nCTEQ15 - Global analysis of nuclear parton distributions with uncertainties in the CTEQ framework, Phys. Rev. D93 (2016) 085037. `arXiv:1509.00792, doi:10.1103/PhysRevD.93.085037`.

[23] K. J. Eskola, P. Paakkinen, H. Paukkunen, C. A. Salgado, EPPS16: Nuclear parton distributions with LHC data, Eur. Phys. J. C77 (3) (2017) 163. `arXiv:1612.05741, doi:10.1140/epjc/s10052-017-4725-9`.

[24] A. H. Mueller, J.-w. Qiu, Gluon Recombination and Shadowing at Small Values of x, Nucl. Phys. B 268 (1986) 427–452. `doi:10.1016/0550-3213(86)90164-1`.

[25] F. Gelis, E. Iancu, J. Jalilian-Marian, R. Venugopalan, The Color Glass Condensate, Ann. Rev. Nucl. Part. Sci. 60 (2010) 463–489. `arXiv:1002.0333, doi:10.1146/annurev.nucl.010909.083629`.

[26] F. Arleo, R. Kolevatov, S. Peigné, M. Rustamova, Centrality and pT dependence of J/psi suppression in proton-nucleus collisions from parton energy loss, JHEP 05 (2013) 155. `arXiv:1304.0901, doi:10.1007/JHEP05(2013)155`.

[27] R. Vogt, J/ψ production and suppression, Phys. Rept. 310 (1999) 197–260. `doi:10.1016/S0370-1573(98)00074-X`.

[28] E. G. Ferreiro, Excited charmonium suppression in proton–nucleus collisions as a consequence of comovers, Phys. Lett. B749 (2015) 98–103. `arXiv:1411.0549, doi:10.1016/j.physletb.2015.07.066`.

[29] X. Du, R. Rapp, Sequential Regeneration of Charmonia in Heavy-Ion Collisions, Nucl. Phys. A 943 (2015) 147–158. `arXiv:1504.00670, doi:10.1016/j.nuclphysa.2015.09.006`.

[30] X. Du, R. Rapp, In-Medium Charmonium Production in Proton-Nucleus Collisions, JHEP 03 (2019) 015. `arXiv:1808.10014, doi:10.1007/JHEP03(2019)015`.

[31] K. H. Ackermann, et al., STAR detector overview, Nucl. Instrum. Meth. A499 (2003) 624–632. `doi:10.1016/S0168-9002(02)01960-5`.

[32] M. L. Miller, K. Reygers, S. J. Sanders, P. Steinberg, Glauber modeling in high energy nuclear collisions, Ann. Rev. Nucl. Part. Sci. 57 (2007) 205–243. `arXiv:nucl-ex/0701025`, `doi:10.1146/annurev.nucl.57.090506.123020`.

[33] J. Adams, et al., Transverse momentum and collision energy dependence of high p(T) hadron suppression in Au+Au collisions at ultrarelativistic energies, Phys. Rev. Lett. 91 (2003) 172302. `arXiv:nucl-ex/0305015`, `doi:10.1103/PhysRevLett.91.172302`.

[34] A. Adare, et al., Ground and excited charmonium state production in $p+p$ collisions at $\sqrt{s} = 200$ GeV, Phys. Rev. D85 (2012) 092004. `arXiv:1105.1966`, `doi:10.1103/PhysRevD.85.092004`.

[35] W. J. Llope, et al., The STAR Vertex Position Detector, Nucl. Instrum. Meth. A759 (2014) 23–28. `arXiv:1403.6855`, `doi:10.1016/j.nima.2014.04.080`.

[36] L. Ruan, et al., Perspectives of a Midrapidity Dimuon Program at the RHIC: A Novel and Compact Muon Telescope Detector, J. Phys. G36 (2009) 095001. `arXiv:0904.3774`, `doi:10.1088/0954-3899/36/9/095001`.

[37] M. Anderson, et al., The Star time projection chamber: A unique tool for studying high multiplicity events at RHIC, Nucl. Instrum. Meth. A499 (2003) 659–678. `arXiv:nucl-ex/0301015`, `doi:10.1016/S0168-9002(02)01964-2`.

[38] M. Beddo, et al., The STAR barrel electromagnetic calorimeter, Nucl. Instrum. Meth. A499 (2003) 725–739. `doi:10.1016/S0168-9002(02)01970-8`.

[39] L. Adamczyk, et al., Measurements of D^0 and D^* Production in $p + p$ Collisions at $\sqrt{s} = 200$ GeV, Phys. Rev. D 86 (2012) 072013. `arXiv:1204.4244`, `doi:10.1103/PhysRevD.86.072013`.

[40] T. C. Huang, et al., Muon Identification with Muon Telescope Detector at the STAR Experiment, Nucl. Instrum. Meth. A833 (2016) 88–93. `arXiv:1601.02910`, `doi:10.1016/j.nima.2016.07.024`.

[41] H. Bichsel, A method to improve tracking and particle identification in TPCs and silicon detectors, Nucl. Instrum. Meth. A562 (2006) 154–197. `doi:10.1016/j.nima.2006.03.009`.

[42] R. Brun, F. Bruyant, M. Maire, A. C. McPherson, P. Zanarini, GEANT3, CERN-DD-EE-84-1.

[43] J. Adam, et al., Measurement of inclusive J/ψ polarization in $p+p$ collisions at $\sqrt{s}$ =200 GeV by the STAR experiment, Phys. Rev. D 102 (9) (2020) 092009. `arXiv:2007.04732`, `doi:10.1103/PhysRevD.102.092009`.

[44] T. Sjostrand, S. Mrenna, P. Z. Skands, PYTHIA 6.4 Physics and Manual, JHEP 05 (2006) 026. `arXiv:hep-ph/0603175`, `doi:10.1088/1126-6708/2006/05/026`.

[45] T. Sjostrand, S. Mrenna, P. Z. Skands, A Brief Introduction to PYTHIA 8.1, Comput. Phys. Commun. 178 (2008) 852–867. `arXiv:0710.3820`, `doi:10.1016/j.cpc.2008.01.036`.

[46] X.-N. Wang, M. Gyulassy, HIJING: A Monte Carlo model for multiple jet production in p p, p A and A A collisions, Phys. Rev. D44 (1991) 3501–3516. `doi:10.1103/PhysRevD.44.3501`.

[47] P. Z. Skands, Tuning Monte Carlo Generators: The Perugia Tunes, Phys. Rev. D82 (2010) 074018. `arXiv:1005.3457`, `doi:10.1103/PhysRevD.82.074018`.

[48] STAR HF tune.
URL https://www.star.bnl.gov/protected/heavy/ullrich/pythia8/

[49] J. Adam, et al., J/ψ production cross section and its dependence on charged-particle multiplicity in $p + p$ collisions at $\sqrt{s} = 200$ GeV, Phys. Lett. B786 (2018) 87–93. arXiv:1805.03745, doi:10.1016/j.physletb.2018.09.029.

[50] R. Ansorge, et al., Charged Particle Multiplicity Distributions at 200-GeV and 900-GeV Center-Of-Mass Energy, Z. Phys. C 43 (1989) 357. doi:10.1007/BF01506531.

[51] B. Alver, et al., Charged-particle multiplicity and pseudorapidity distributions measured with the PHOBOS detector in Au+Au, Cu+Cu, d+Au, and p+p collisions at ultrarelativistic energies, Phys. Rev. C 83 (2011) 024913. arXiv:1011.1940, doi:10.1103/PhysRevC.83.024913.

[52] G. D. Lafferty, T. R. Wyatt, Where to stick your data points: The treatment of measurements within wide bins, Nucl. Instrum. Meth. A355 (1995) 541–547. doi:10.1016/0168-9002(94)01112-5.

[53] Y.-Q. Ma, R. Vogt, Quarkonium Production in an Improved Color Evaporation Model, Phys. Rev. D94 (11) (2016) 114029. arXiv:1609.06042, doi:10.1103/PhysRevD.94.114029.

[54] Y.-Q. Ma, R. Venugopalan, K. Watanabe, H.-F. Zhang, $\psi(2S)$ versus J/ψ suppression in proton-nucleus collisions from factorization violating soft color exchanges, Phys. Rev. C97 (1) (2018) 014909. arXiv:1707.07266, doi:10.1103/PhysRevC.97.014909.

[55] J.-P. Lansberg, H.-S. Shao, Towards an automated tool to evaluate the impact of the nuclear modification of the gluon density on quarkonium, D and B meson production in proton–nucleus collisions, Eur. Phys. J. C77 (1) (2017) 1. arXiv:1610.05382, doi:10.1140/epjc/s10052-016-4575-x.

[56] A. Kusina, J.-P. Lansberg, I. Schienbein, H.-S. Shao, Gluon Shadowing in Heavy-Flavor Production at the LHC, Phys. Rev. Lett. 121 (5) (2018) 052004. `arXiv:1712.07024, doi:10.1103/PhysRevLett.121.052004`.

[57] H.-S. Shao, HELAC-Onia 2.0: an upgraded matrix-element and event generator for heavy quarkonium physics, Comput. Phys. Commun. 198 (2016) 238–259. `arXiv:1507.03435, doi:10.1016/j.cpc.2015.09.011`.

[58] H.-S. Shao, HELAC-Onia: An automatic matrix element generator for heavy quarkonium physics, Comput. Phys. Commun. 184 (2013) 2562–2570. `arXiv:1212.5293, doi:10.1016/j.cpc.2013.05.023`.

[59] S. Dulat, T.-J. Hou, J. Gao, M. Guzzi, J. Huston, P. Nadolsky, J. Pumplin, C. Schmidt, D. Stump, C. P. Yuan, New parton distribution functions from a global analysis of quantum chromodynamics, Phys. Rev. D93 (3) (2016) 033006. `arXiv:1506.07443, doi:10.1103/PhysRevD.93.033006`.

[60] M. Cacciari, M. Greco, P. Nason, The P(T) spectrum in heavy flavor hadroproduction, JHEP 05 (1998) 007. `arXiv:hep-ph/9803400, doi:10.1088/1126-6708/1998/05/007`.

[61] M. Cacciari, S. Frixione, P. Nason, The p(T) spectrum in heavy flavor photoproduction, JHEP 03 (2001) 006. `arXiv:hep-ph/0102134, doi:10.1088/1126-6708/2001/03/006`.

[62] K. J. Eskola, H. Paukkunen, C. A. Salgado, EPS09: A New Generation of NLO and LO Nuclear Parton Distribution Functions, JHEP 04 (2009) 065. `arXiv:0902.4154, doi:10.1088/1126-6708/2009/04/065`.